Optimize the Mechanical Properties of $Al_{0.6}CoCrFeNi$ High-Entropy Alloys by Thermo-Mechanical Processing

Huijun Yang [1], Yaqin Tan [1], Junwei Qiao [1,*], Jeffrey A. Hawk [2], Yong Zhang [3], Michael Gao [2,4,*] and Peter K. Liaw [5]

[1] Laboratory of High-Entropy Alloys, College of Materials Science and Engineering, Taiyuan University of Technology, Taiyuan 030024, China; pineyang@126.com (H.Y.); tanyaqin@tyut.edu.cn (Y.T.)
[2] National Energy Technology Laboratory, 1450 Queen Ave SW, Albany, OR 97321, USA; Jeffrey.hawk@netl.doe.gov
[3] State Key Laboratory for Advanced Metals and Materials, University of Science and Technology Beijing, Beijing 100083, China; drzhangy@ustb.edu.cn
[4] Department of Leidos Research Support Team, 1450 Queen Ave SW, Albany, OR 97321, USA
[5] Department of Materials Science and Engineering, The University of Tennessee, Knoxville, TN 37996, USA; pliaw@utk.edu
[*] Correspondence: qiaojunwei@gmail.com (J.Q.); mcgao07@gmail.com (M.G.)

Abstract: The phase stability, microstructural evolution, and mechanical properties of $Al_{0.6}CoCrFeNi$ high-entropy alloy (HEA) subjected to different thermo-mechanical treatments were systematically investigated in the present study. The face center cubic (FCC) matrix, B2, and minor Body Center Cubic (BCC) phases were observed in the as-cast state. The morphology of the B2 precipitates evolved from needle-like to droplet-shaped when annealed at 900 °C, 1000 °C, and 1100 °C. The resulting yield stress of this FCC/B2 duplex-phase HEA after annealing heat treatments was successfully analyzed based on the contributions from solid solution strengthening, precipitate strengthening, grain boundary hardening, and dislocation hardening.

Keywords: high-entropy alloy; thermo-mechanical treatment; microstructure; phase stability; strengthening mechanisms

1. Introduction

The underlying concept of high-entropy alloys (HEAs) opens a vast pallet of possible chemistries for alloy design and has, as a consequence, attracted tremendous research interest since 2004 [1–6]. The term HEA was defined by Yeh to mean that a high-entropy alloy consists of at least five principal elements in equimolar, or near-equimolar, the ratio with atomic concentrations ranging from 5% to 35% for each element and is located near the center of a multi-component phase diagram. The high configurational entropy of the alloy can lead to the formation of solid solutions with the face-centered-cubic (FCC) crystal structure [7], body-centered-cubic (BCC) crystal structure [8], or hexagonal-close-packed (HCP) crystal structure [9]. Many extraordinary properties of HEAs were reported: Instances of extremely high fracture toughness [10], superior corrosion resistance [11], high thermal stability [12], good wear and fatigue resistance [13,14], and excellent superconductivity [15]. Great efforts are underway to investigate the formation of simple solid solution HEAs and to understand their physical and mechanical properties [16–18]. However, single-phase HEAs have limited applications especially for structural materials. For example, HEAs with the FCC crystal structure are very ductile but the yield stress is low, while HEAs with the BCC crystal structure are stronger but with limited ductility. Accordingly, doping/alloying (e.g., $Al_xCoCrFeNi$) and/or utilizing thermo-mechanical processing can balance the strength–ductility of structural HEAs. This often results in the formation of multi-phase and/or multi-scale microstructures [19–21]. Consequently, a variety of

strengthening mechanisms can be designed into the HEA to improve strength, including using precipitation hardening [22], grain refinement [23], and dislocation hardening [24].

The Al_xCoCrFeNi (where *x* signifies the molar ratio of Al) alloy has been extensively studied in terms of microstructures that develop as well as the physical and mechanical properties that result [25–28]. The alloy basically manifests as a FCC crystal structure when *x* < 0.45, as a dual-phase (FCC + BCC) structure when 0.45 < *x* < 0.88, and as a BCC crystal structure when *x* > 0.88 [29]. However, to date, there have been limited studies on using thermo-mechanical processing to optimize the mechanical properties of dual-phase Al_xCoCrFeNi HEA. The objective of the present study is to understand the effects that cold rolling and subsequent annealing have on the microstructure and the resulting mechanical properties of the $Al_{0.6}$CoCrFeNi HEA and to quantitatively predict the yield stress of the HEA by analyzing the roles of different strengthening mechanisms.

2. Experiments

The HEA ingots possessed a nominal composition of $Al_{0.6}$CoCrFeNi. These ingots were prepared by arc melting a pure elemental mixture (element purity greater than 99.9 weight percent (wt. %)) in a high-purity argon atmosphere. The ingots were remelted at least four times to improve chemical homogeneity before being drop-cast into a water-cooled copper mold with dimensions of 85 mm × 10 mm × 2 mm. The ingots were directly cold-rolled by 40% (1.2 mm thickness) at room temperature and then subsequently annealed at 900 °C, 1000 °C, and 1100 °C for 1 h and 2 h, respectively, before water-quenching.

The phases in the alloys were identified by X-ray diffraction (XRD) (Rigaku TTRIII diffractometer using Cu Kα radiation with a scanning step of 0.02° from 20 to 100 degrees) (Rigaku, Tokyo, Japan). The CALPHAD (CALculation of PHAse Diagrams) simulation was performed using the PanHEA database supplied by CompuTherm^{TM} [30] to predict phase stability. The microstructure was examined optically using a Leica DM2700M microscope (OM, Leica, Weztlar, Germany). Scanning electron microscopy (SEM, TESCAN, BrNo, Czech Republic) was performed on a Miras Tescan SEM equipped with the energy-dispersive spectrometer (EDS, Oxford, UK). Transmission electron microscopy (TEM) was performed on a JEM-F200 TEM (JEOL, Tokyo, Japan). TEM samples started with 3 mm diameter punched discs which were then ground to about 30 μm thickness. At this point, the 3 mm diameter discs were ion milled using Model 691 Gatan precision ion polishing system. Electron-backscatter-diffraction imaging (EBSD) was performed on a Hitachi S-3400N SEM equipped with an HKL-EBSD system (Hitachi, Japan).

Tensile specimens were dog-bone-shaped. Specimens were made by electrical discharge machining (EDM, Zhongxing numerical control machine tool, Taizhou, China) with a gauge length of 10 mm, gauge width of 4 mm, and gauge thickness of 2 mm, or 1.2 mm, in the as-cast and the cold-rolled conditions, respectively. Tension testing was performed using an Instron 5969 Universal Testing System at room temperature using a strain rate of 1×10^{-3}/s. The surfaces of the gauge section of the tensile specimens were polished to 2000 grit (~9.5 μm) finish on SiC paper to eliminate surface scratches. Four tensile tests were performed for each condition (cast/cold-rolled, heat treatment temperature, heat treatment time). Nanoindentation hardness testing was conducted using a load of 0.2 gf with 10 s dwell time to acquire statistics on the nanoindentation hardness of each phase.

3. Results

3.1. Phase Identification

The XRD results of the $Al_{0.6}$CoCrFeNi HEA in the as-cast, cold-rolled, and annealed states are shown in Figure 1. The as-cast $Al_{0.6}$CoCrFeNi HEA is composed of FCC and BCC/B2 phases. Here BCC refers to a disordered BCC phase while B2 refers to an ordered NiAl-type BCC phase demonstrated by the presence of (100) diffraction peak. From XRD results, it did not detect any new phases after subsequent thermo-mechanical treatments. The lattice constants determined from XRD are 0.359 nm for the FCC phase and 0.288 nm for the BCC/B2 phase. These values did not change under the different processing conditions.

Note that XRD analysis cannot precisely differentiate the volume fractions of the BCC and B2 phases because of overlapping peaks.
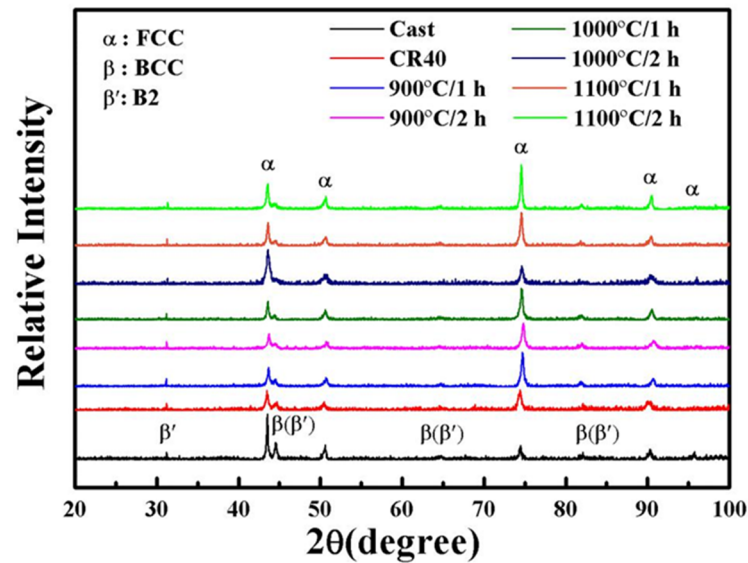

Figure 1. XRD patterns of the Al$_{0.6}$CoCrFeNi HEA in the as-cast, 40% cold-rolled (CR40), and various HT variants.

The calculated phase diagrams are presented in Figure 2. The database predicts the formation of primary FCC solid solutions with the B2 phase during solidification. The predicted equilibrium mole fractions of FCC and B2 structures are 75% and 25% at 900 °C, 78% and 22% at 1000 °C, and 82% and 18% at 1100 °C, respectively (see Table 1). The database predicts that the phase forms at ~868 °C and the disordered BCC phase forms at ~612 °C at equilibrium conditions. Due to sluggish diffusion, the phase does not form at the as-cast state or under short-time annealing. On the other hand, the non-equilibrium solidification (i.e., no diffusion in the solid-state) predicts the formation of major FCC phase, B2 phase and minor disordered BCC phase in the as-cast state.
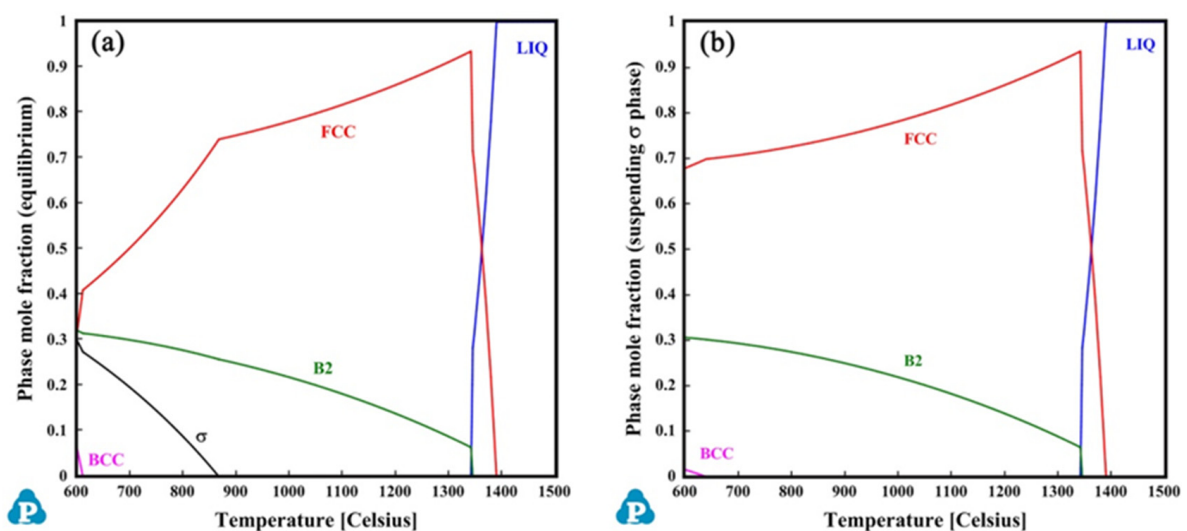

Figure 2. *Cont*.
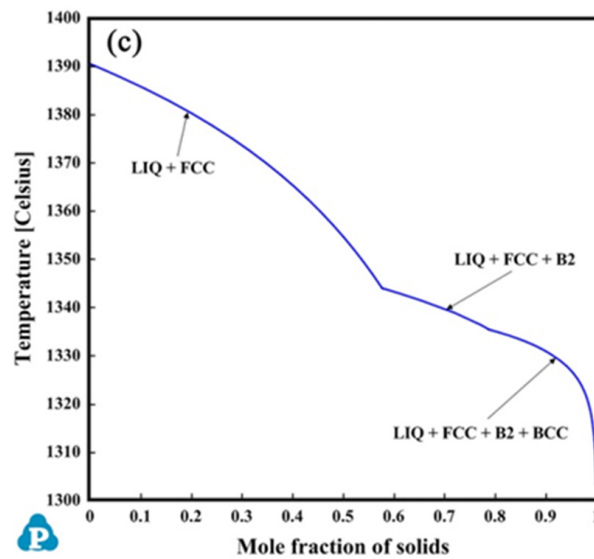
Figure 2. CALPHAD-predicted phase diagram for $Al_{0.6}CoCrFeNi$ HEAs using the PanHEA database [30]: (**a**) Equilibrium, (**b**) suspending phase, and (**c**) Scheil solidification [31].

Table 1. The volume fraction (%) of each phase of $Al_{0.6}CoCrFeNi$ HEAs in different states evaluated from microstructural observations. The predicted equilibrium mole fractions of phases from CALPHAD are also provided.

Condition	Phase	As-Cast	900 °C/1 h	1000 °C/1 h	1100 °C/1 h	900 °C/2 h	1000 °C/2 h	1100 °C/2 h
Experiment (volume percent)	FCC	~67	~73	~77	~79	~75	~77	~81
	B2	~19	~17	~16	~21	~25	~22	~19
	BCC	~14	~10	~7	~0	~0	~0	~0
CALPHAD (mole percent)	FCC		75	78	82	75	78	82
	B2		25	22	18	22	22	18

3.2. Microstructure Evolution

The SEM microstructures of the $Al_{0.6}CoCrFeNi$ HEA in the as-cast, cold-rolled and annealed states are exhibited in Figure 3. The microstructure in the as-cast state consists of the FCC phase in the dendrite arms (bright color) and the BCC/B2 phase in the inter-dendritic regions. The BCC/B2 microstructure appears as a weave-like structure (Figure 3b), suggesting possible spinodal decomposition [32,33]. Figure 3c shows the microstructure of the 40% cold-rolled alloy variant. XRD did not detect any new phase forming after cold rolling. Figure 3d–f (and Figure 3g–i) show the microstructures of the alloys after annealing for 1 h (and 2 h) at 900 °C, 1000 °C, and 1100 °C, respectively. Compared with the cold-rolled alloys, the 900 °C/1 h and 1000 °C/1 h annealed alloys have similar morphologies to the as-cast state, with some needle-like precipitates distributed in the dendritic region.

The precipitates are further characterized in SEM micrographs as B2 phase with a thickness of about 60 nm and a width between 0.2 and 0.6 μm (see Figure 3d,e). Selected-area-electron-diffraction (SAED) from TEM observations provided strong confirmation (Figure 4). The inter-dendritic regions after annealing at 1000 °C shrank by ≥50% compared to similar regions annealed at 900 °C, indicating a decreasing amount of disordered BCC phase. For the 1100 °C/1 h annealed alloy (Figure 3f), the morphology of the B2 phase evolved into a droplet shape with inter-dendritic regions disappearing. Increasing the annealing time to 2 h caused an increase in grain size of B2 phases but no further change in B2 morphology.
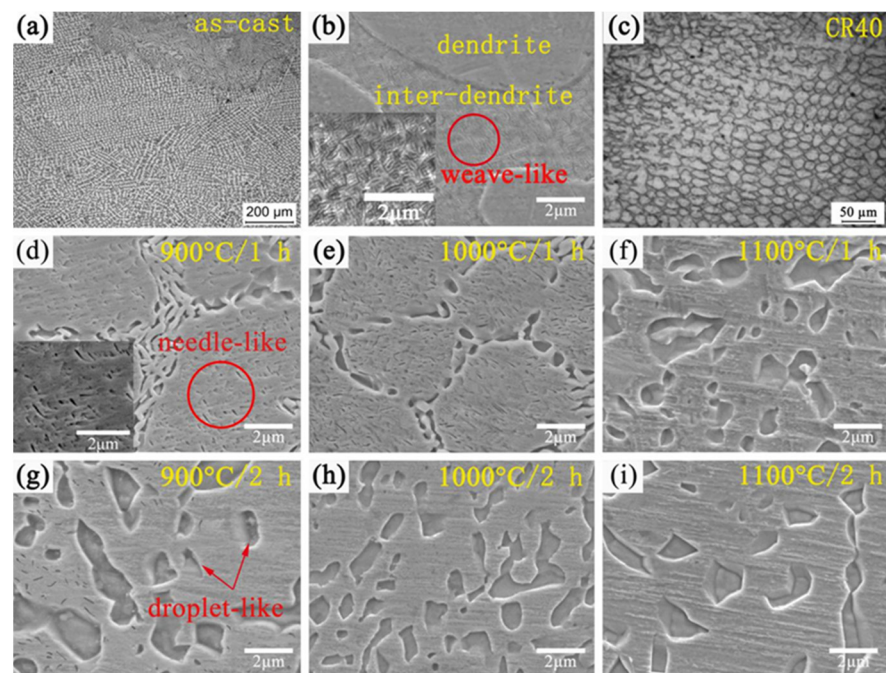
Figure 3. Microstructure of $Al_{0.6}CoCrFeNi$ HEA in the as-cast (**a**,**b**), CR40 (**c**), 1 h-annealed (**d**–**f**) variants and 2 h-annealed (**g**–**i**) variants at 900 °C, 1000 °C, and 1100 °C, respectively, where (**a**,**c**) are OM pictures, and the rest are SEM images.

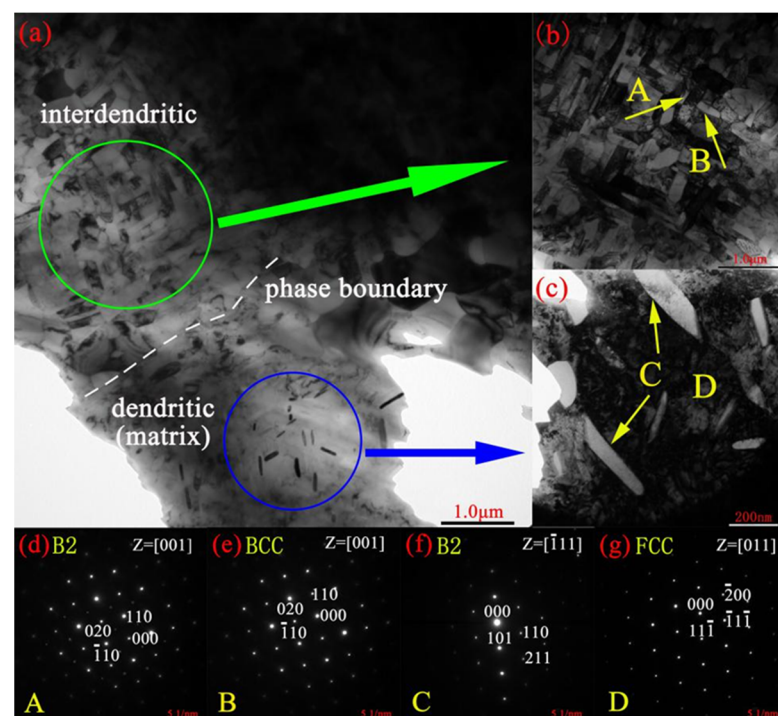**Figure 4.** Decomposition of BCC into B2 phase and precipitation of B2 phase in $Al_{0.6}CoCrFeNi$ HEAs after annealing at 900 °C for 1 h. (**a**) The bright field TEM image of. (**b**) Decomposed B2 (marked as A) and BCC phase (marked as B). (**c**) B2 precipitation in FCC matrix (marked by C) embedded in the FCC matrix (marked by D). (**d**–**g**) The corresponding SAED (selected area electron diffraction) patterns of area A, B, C, and D marked in (**b**,**c**).

The estimated volume fractions of the FCC and BCC/B2 phases for the different thermomechanical processing (TMP) + heat treatment (HT) variants are also listed in

Table 1, together with predictions from equilibrium phase diagrams via CALPHAD. With increasing annealing temperature (i.e., from 900 °C to 1000 °C to 1100 °C), the volume fraction of the FCC phase increases slightly while the volume fraction of the B2 phase decreases slightly. The disordered BCC phase fraction gradually decreased from about 15% in the as-cast state to zero at T ≥ 1000 °C. The observed phase evolution agrees well with CALPHAD predictions (see Figure 2). Figure 5 shows the EDS results from inspection of $Al_{0.6}CoCrFeNi$ HEAs in the as-cast and annealed states. The FCC phase is enriched with Fe and Cr while the B2 phase is enriched in Al and Ni. The corresponding chemical composition of FCC and B2 phases in the different variants are listed in Table 2.
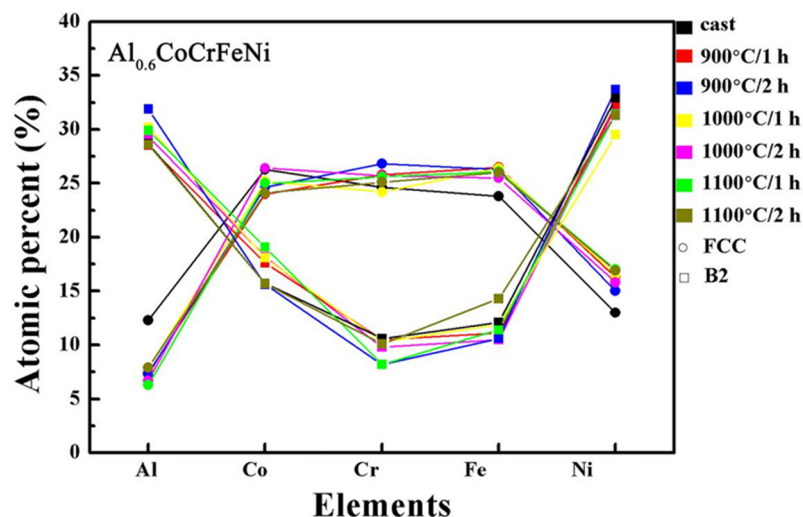

Figure 5. The EDS results of FCC and B2 phases in $Al_{0.6}CoCrFeNi$ HEAs in the as-cast and various annealed variants.

Table 2. The average composition (at. %) of FCC and BCC/B2 phases of $Al_{0.6}CoCrFeNi$ HEAs in various variants.

States	Phase	Al	Co	Cr	Fe	Ni
As-cast	FCC	12.7	25.9	24.6	23.8	13
	BCC	11.5	17.3	36.2	25.9	9.1
	B2	29.4	18.2	9.8	10.5	32.1
900 °C/1 h	FCC	7.4	24.0	25.8	25.9	17.3
	BCC	11.9	18.6	33.6	26.3	9.6
	B2	28.5	17.6	10.5	11.1	32.3
900 °C/2 h	FCC	7.3	24.6	26.8	26.8	14.5
	B2	31.9	15.6	8.2	10.6	33.7
1000 °C/1 h	FCC	7.9	25.2	24.2	26.4	16.5
	BCC	12.8	18.1	32.5	26.8	9.8
	B2	30.2	18.1	10.3	11.9	29.5
1000 °C/2 h	FCC	6.7	26.4	25.7	25.5	15.8
	B2	28.7	15.7	10.6	12.1	32.9
1100 °C/1 h	FCC	6.3	24.5	25.6	26.1	17.5
	B2	28.9	20.1	8.2	11.4	31.4
1100 °C/2 h	FCC	7.9	24.1	25.1	26.0	16.9
	B2	28.6	15.7	10.1	14.3	31.3

3.3. EBSD Characterizations

Figure 6 present the EBSD maps of $Al_{0.6}CoCrFeNi$ HEAs in the 900 °C/1 h, and 1100 °C/2 h annealed states, respectively. Subjected to heavy plastic deformation, it is

difficult to distinguish the complete grains for CR40 samples. The average grain size of 900 °C/1 h, and 1100 °C/2 h alloy variants is 14 μm and 7 μm, respectively. The needle-like and droplet-like B2 precipitates were observed in the 900 °C/1 h (Figure 6(a1)) and 1100 °C/2 h annealed variants (Figure 6(b1)).
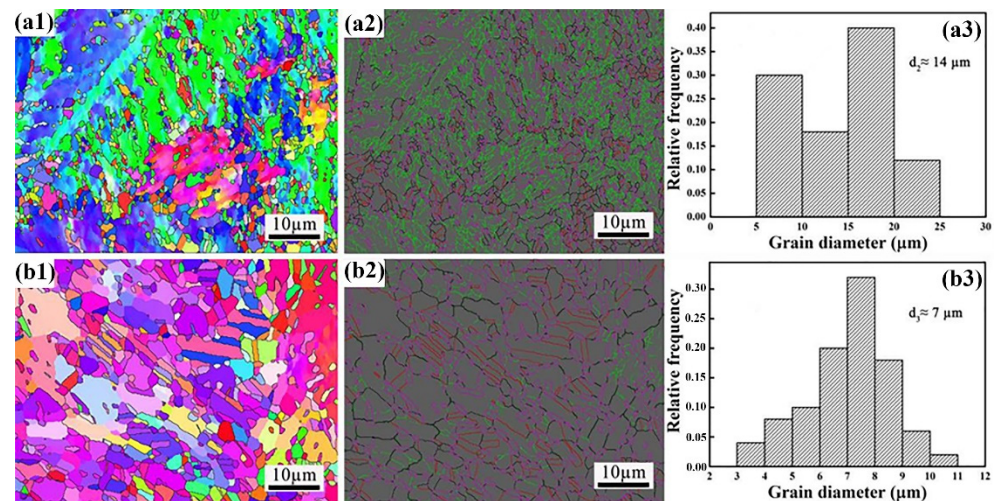

Figure 6. EBSD maps of $Al_{0.6}CoCrFeNi$ HEA in the 900 °C/1 h (**a1**), and 1100 °C/2 h (**b1**) annealed variants, and the corresponding grain-boundary maps (**a2,b2**) and grain size distributions (**a3,b3**). The black, green purple, and red colors in (**a2,b2**) represent high-angle grain boundaries, low-angle grain boundaries, interphase boundaries, and twin boundaries, respectively.

Furthermore, the corresponding grain-boundary maps for each state, including the high-angle grain boundaries, low-angle grain boundaries, twin boundaries, and interphase boundaries are shown in Figure 6(a2,b2). Recovery and partial recrystallization occurred in the 900 °C/1 h annealed state (Figure 6(a2)) because many low-angle boundaries and a small quantity of high-angle grain boundaries remained in the alloy. For the 1100 °C/2 h annealed (Figure 6(b2)) variant, low-angle grain boundaries were replaced by high-angle grain boundaries (≥80%), meaning that full recrystallization took place [34]. A large number of twins, represented by red lines in the plot, were observed in all samples. The twin spacing in the CR40 alloy is about 8 μm and decreases to 3–4 μm after annealing at 900 °C/1 h or 1100 °C/2 h. As expected, deformation twins developed in the CR40 alloy. Whereas for the 900 °C/1 h and 1100 °C/2 h annealed states, three typical annealing twins formed: (1) Twins at the intersection of grain boundaries, (2) complete twins across the whole grain, and (3) incomplete twins terminated within the grain with one end [35].

3.4. Mechanical Properties

Figure 7a shows the representative tensile stress–strain curves of $Al_{0.6}CoCrFeNi$ HEA variants subject to different processing (TMP + HT) conditions. The yield stress in the as-cast state was 360 MPa. It increased to 1.2 GPa after cold-rolling. As expected, increasing the annealing temperatures or increasing annealing time at a fixed temperature promotes tensile ductility but reduces the yield stress and fracture strength. Annealing at 1000 °C for 1 h yields an optimal balance of yield stress (886 MPa) and elongation (20%). Annealing for 2 h at 900–1100 °C deteriorates the mechanical properties of the alloy.
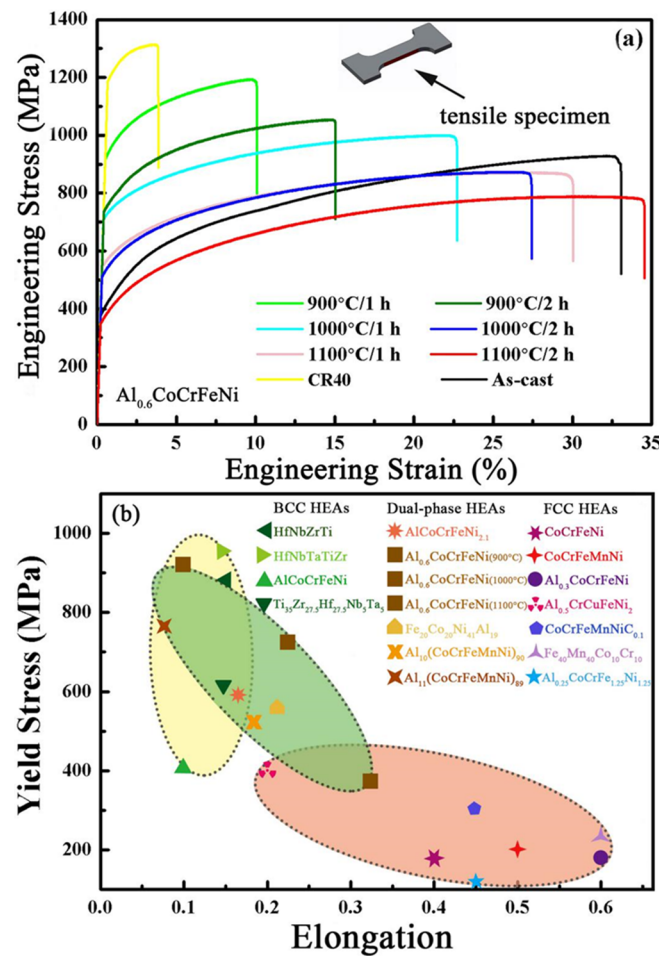
Figure 7. (**a**) The engineering tensile stress–strain curves of $Al_{0.6}CoCrFeNi$ HEA after annealing at 900 °C, 1000 °C, and 1100 °C for 1 and 2 h, compared with the results from the as-cast and cold-rolled states. (**b**) Tensile yield stress versus elongation for $Al_{0.6}CoCrFeNi$ HEA after HT at 900 °C, 1000 °C, and 1100 °C for 1h compared with other HEAs in the as-cast state.

Figure 7b compares the tensile yield stress and elongation of the dual-phase $Al_{0.6}CoCrFeNi$ HEA in the present study with other HEAs (with FCC, FCC + BCC dual-phase, and BCC structures) reported in the literature. The present $Al_{0.6}CoCrFeNi$ HEA in the 900 °C/1 h variant exhibits balanced mechanical properties, i.e., good yield stress and good ductility. In contrast, those BCC refractory HEAs (e.g., HfNbZrTi [36], HfNbTaTiZr [37], AlCoCrFeNi [38] and $Ti_{35}Zr_{27.5}Hf_{27.5}Nb_5Ta_5$ [39]) have higher yield stress but with much lower ductility than $Al_{0.6}CoCrFeNi$. On the other hand, those FCC HEAs (e.g., CoCrFeNi [40], CoCrFeMnNi [41], $Al_{0.3}CoCrFeNi$ [42], $Al_{0.5}CrCuFeNi_2$ [43], $CoCrFeMnNiC_{0.1}$ [41], $Fe_{40}Mn_{40}Co_{10}Cr_{10}$ [44], $Al_{0.25}CoCrFe_{1.25}Ni_{1.25}$ [45]) are very ductile but their mechanical strength are very low. Compared to other dual-phase FCC + BCC HEAs such as $AlCoCrFeNi_{2.1}$ [46], $Fe_{20}Co_{20}Ni_{41}Al_{19}$ [47], $Al_{10}(CoCrFeMnNi)_{90}$ [48], and $Al_{11}(CoCrFeMnNi)_{89}$ [48], the present $Al_{0.6}CoCrFeNi$ HEA has lower yield stress and larger elongation, but overall their mechanical properties are similar. Since TMP + HT can alter the mechanical performance of an alloy significantly, the comparison as shown in Figure 6b can only be used as a guide.

The measured nanoindentation test results for the FCC phase, B2 phase and the alloy are shown in Figure 8. As expected, the B2 phase has much higher hardness than the FCC phase at a fixed temperature. For the 1 h and 2 h HT variants, overall hardness for the alloy decreases with increasing annealing temperature, following the trend of the FCC phase. This is because the FCC phase is the dominant phase in the microstructure (i.e., phase fraction > 3:1 for FCC to B2). The product of volume fraction and the corresponding nano-hardness of B2 and FCC phases for the alloy in various HT variants is shown in Figure 9.
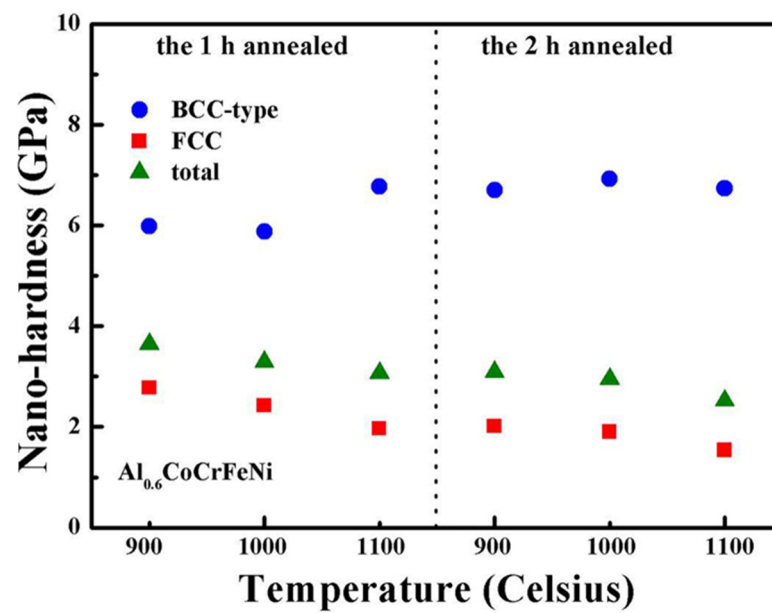
Figure 8. The measured nanoindentation hardness values of $Al_{0.6}CoCrFeNi$ HEA after annealed from 900 °C/1 h to 1100 °C/2 h.
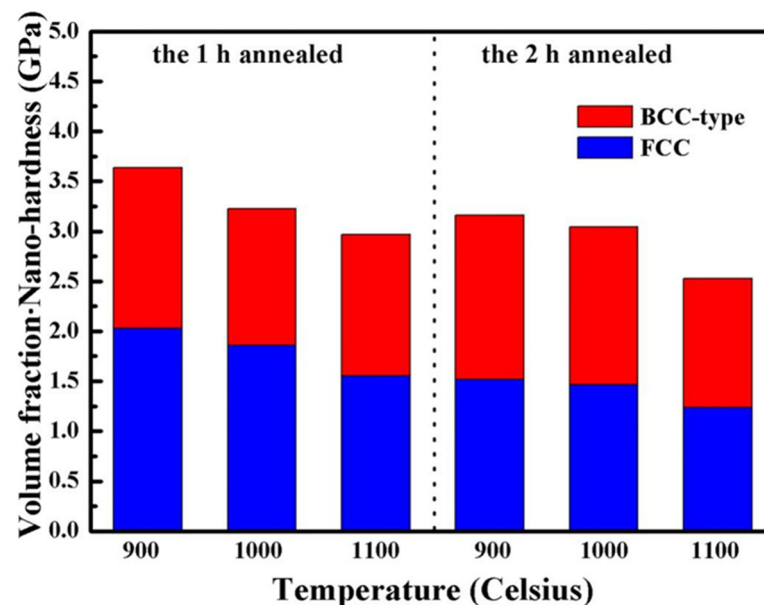

Figure 9. The nanoindentation hardness partition of FCC and BCC-type phases for the total nanoindentation hardness in different states using the RoM.

4. Discussions

4.1. Twins and Deformation Mechanisms of FCC and BCC Phases

The EBSD maps (Figure 6) provide interesting insight. For example, the twins observed in the HEAs are $\sum 3$ (i.e., 60° at <111>), which is typically observed in TWIP steels [49,50], TRIP steel [51] and other FCC-structured alloys [52,53]. Both deformation twins and annealing twins depend on the nature of crystal structures and stacking fault energy, however, their twinning processes are totally different. For the CR40 variant, dislocation slip was hindered by secondary phases and grain boundaries in the FCC crystal during uniform deformation. Deformation twins would be activated when the stress arrived at the critical twins shear stress [54]. In contrast, annealing heat treatment leading to recovery (and recrystallization) promotes annihilation of deformation twins because low energy

boundaries such as twin boundaries can migrate through the FCC phase until it meets a high angle boundary [55]. Thus, annealing twins cannot be considered as a strengthening source and is ignored in the following yield stress calculation.

The FCC and BCC/B2 phases contribute very differently to the deformation behavior of the alloy. Regardless of how the twin was formed (i.e., deformation twins or annealing twins), they only exist within the FCC phases, agreeing with a prior study by Rao et al. [56]. Bönisch et al. [57] studied the compression behavior of $Al_{0.5}CoCrFeNi$ HEA that was also comprised of FCC and BCC/B2 phases. Deformation was dominated by the FCC phase at the early stage while BCC/B2 was almost undeformed. At the late stage, only multiple slip systems were activated in the BCC/B2 phase and even large amounts of deformation bands and deformation twins formed in the FCC phase.

4.2. Strengthening Mechanisms

The yield stress (σ_y) of a precipitation-strengthened alloy may contain various strengthening contributions: (1) strengthening from the solid solution ($\Delta\sigma_s$), (2) strengthening due to dislocations ($\Delta\sigma_d$), (3) strengthening from grain boundaries ($\Delta\sigma_g$), and (4) strengthening from precipitates ($\Delta\sigma_p$) [58]. A simple model that sums all the contributions can be expressed as:

$$\sigma_y = \sigma_0 + \sigma_s + \sigma_d + \sigma_g + \sigma_p \tag{1}$$

where σ_0 is the intrinsic strength (i.e., the lattice friction strength) of the material. In this study, Equation (1) is used to calculate the yield stress of the CR40 and of the 900 °C/1 h and 1100 °C/2 h annealed variants. The details in calculating σ_0, σ_s, σ_d, σ_g and σ_p are in the following sections.

4.2.1. Intrinsic Strength

Following the Peierls–Nabarro stress model [35], the calculated intrinsic yield strength for $Al_{0.6}CoCrFeNi$ HEA are 162 MPa, 160 MPa, and 158 MPa, for the CR40, 900 °C/1 h, and 1100 °C/2 h annealed variants, respectively.

4.2.2. Solid-Solution Strengthening

Analyzing solid-solution hardening (SSH) is often based on traditional dilute alloys [59], especially binary systems [60]. For dilute binary solid solution alloys, the effect of SSH is mainly due to the atomic size mismatch and shear modulus mismatch between the solute and solvent elements. For composition concentrated complex alloys such as equimolar (or near-equimolar) HEAs, evaluation of SSH remains a challenge [61,62] because solute and solvent elements are essentially indistinguishable. For simplicity, the $Al_{0.6}CoCrFeNi$ HEA is considered a "quasi-binary alloy". In this case, Al is the solute with a significantly larger atomic size, while the mixture of CoCrFeNi acts as the solvent since these transition metal elements possess very similar atomic radii and chemical properties.

Equations (2)–(5) can be used to calculate the strengthening effect in a substitutional solid solution model with elastic dislocation-solute interactions [48,59]:

$$\Delta\sigma_s = M \cdot \frac{G \cdot \varepsilon_s^{3/2} \cdot c^{1/2}}{700} \tag{2}$$

where M is the Taylor factor which converts shear stress to normal stress. The Taylor factor is 3.06 [63] for FCC structures and 2.75 for BCC structures. G is the shear modulus and it is estimated as 67 GPa for the FCC phase and 88 GPa for the BCC phase in $Al_{0.6}CoCrFeNi$ HEA. The atomic fraction of Al is c (see Table 2). Finally, ε_s is determined from the elastic mismatch ε_G and atomic size mismatch ε_a:

$$\varepsilon_s = \left| \frac{\varepsilon_G}{1 + 0.5\varepsilon_G} - 3\varepsilon_a \right| \tag{3}$$

Separately, ε_G and ε_a, are defined as:

$$\varepsilon_G = \frac{1}{G} \cdot \frac{\partial G}{\partial c} \tag{4}$$

$$\varepsilon_a = \frac{1}{a} \cdot \frac{\partial a}{\partial c} \tag{5}$$

where a = 0.3578 nm and is the lattice parameter of the CoCrFeNi FCC matrix [22]. The refined lattice parameters for FCC phases in the CR40 and for the 900°C/1 h and 1100°C/2 h annealed variants are 0.3592, 0.3592, and 0.3598 nm, respectively. For the BCC/B2 phases, the lattice parameters are 2.884 nm. Since ε_G is negligible compared to ε_a, $\varepsilon_s \approx |3\varepsilon_a|$.

The total solid solution strengthening contribution to the alloy is calculated using Equation S8, and this results in 189 MPa, 133 MPa, and 5 MPa for the CR40, 900 °C/1 h, and 1100 °C/2 h variants, respectively. For the 900 °C/1 h annealed variant, the volume fraction of the FCC phase increased while the disordered BCC phase decreased. As such the change in phase fraction ratio led to the strength loss. The 1100 °C/2 h annealed variant thus had the lowest strengthening effect among the three variants.

4.2.3. Dislocation Hardening

Intrinsically, stress to the crystal propels mobile dislocations to move. As they interact with other dislocations, the various boundaries in the FCC crystal and other point defects, they multiply, which leads to the substantially enhanced dislocation density, tangled dislocation structures, and dislocation–boundary interactions. As dislocation motion is impeded, the stress required to continue to move the dislocations increases. The resulting increase in stress is defined as work hardening in FCC crystal structures. The effect of dislocation hardening can be calculated using the Bailey–Hirsh relationship [63]:

$$\Delta\sigma_d = M\alpha Gb\rho^{1/2} \tag{6}$$

where α is a constant ($\approx$0.2 for FCC crystals and 0.4 for BCC crystals [63]); G is the shear modulus of the FCC phase (~67 GPa); b is the magnitude of the Burgers vector where $b = \frac{\sqrt{2}}{2} \cdot a = 0.254$ nm for FCC phase in the present study; and ρ represents the dislocation density. It is generally accepted that work-hardened FCC alloys (i.e., cold-worked such as CR40) may contain up to 10^{12} dislocation per cm^2 [64], while in annealed alloys the dislocation density may be between 10^6 to 10^8 dislocations per cm^2, depending upon the FCC alloy composition and the annealing heat treatment [64].

Here, a value of 10^{12}/cm^2 for the holistic dislocation density for FCC phases is adopted for simplicity. Thus, the strengthening effect of the CR40 alloy from dislocation is $\Delta\sigma_{dFCC} \cdot V_{FCC}$. In the 900 °C/1 h annealed alloy, the dislocation density is estimated as 10^{10}/cm^2 considering recovery and partial recrystallization. In the 1100 °C/2 h annealed variant, full recrystallization is assumed to have occurred. As such the dislocation density was estimated as 10^8/cm^2.

It is generally regarded that there is limited dislocations motion during plastic deformation in B2-type intermetallic with limited measured ductility [65]. Given the nature of the B2 crystal structure, it is difficult for dislocations to nucleate and propagate. Therefore, work hardening contribution, i.e., dislocation hardening, in the B2 and BCC phases of the Al$_{0.6}$CoCrFeNi HEA in the cold-rolled state is ignored.

Using these approximations of dislocation densities for the Al$_{0.6}$CoCrFeNi in various HT variants, the contributions to yield stress from dislocation strengthening are 698 MPa, 240 MPa, and 8 MPa for the CR40, 900°C/1 h, 1100°C/2 h HEA variants, respectively. Dislocation strengthening constitutes a major contribution to the yield stress in the CR40 alloy but decreases substantially for the annealed variants due to the dramatic reduction in dislocation densities resulting from annealing heat treatment.

4.2.4. Grain-Boundary Strengthening

Grain boundaries (GB) are barriers to dislocation motion. Both GB and twin boundary (TB) strengthening follow the Hall–Petch relationship [59,63]:

$$\Delta\sigma_g = k_g \cdot d^{-1/2} + k_t \cdot \lambda^{-1/2} \tag{7}$$

where k_g is the proportionality constant ($\approx$226 and 617 MPa $\cdot \sqrt{\mu m}$ for FCC and BCC/B2 phases [66,67], respectively). The value for k_g was determined as 335, 286, and 226 MPa $\cdot \sqrt{\mu m}$ by RoM for the CR40, 900 °C/1 h and 1100 °C/2 h variants, respectively. The variable k_t is set to 226 MPa $\cdot \sqrt{\mu m}$ [59], while d is the average grain diameter. The variable λ is the average twin boundary spacing. The calculated $\Delta\sigma_g$ values are 159 MPa, 76 MPa, and 85 MPa for the CR40, 900 °C/1 h, 1100 °C/2 h variants, respectively.

4.2.5. Secondary-Phase Hardening

The BCC/B2 phase decomposed and transformed into nanometer-sized or even micrometer-sized B2 dispersed in the FCC matrix during the annealing heat treatments at 900 °C, 1000 °C, and 1100 °C (see Figure 4) in $Al_{0.6}CoCrFeNi$ HEAs in the present study. Therefore, hardening by discrete precipitates should be considered. Deformation in precipitate strengthened alloys takes place either by a dislocation shearing mechanism if the size of the precipitate is smaller than a critical radius (r_{crit}), or by Orowan looping mechanism if the size of the precipitate is greater than a critical radius, r_{crit} [58,59,68]. The precipitation strengthening in the present study is assumed to occur by the Orowan looping mechanism since the calculations assuming the shearing mechanism results in unrealistic yield strength.

The Orowan looping mechanism produces an increment of the yield stress according to the following equation [59,68]:

$$\Delta\sigma_{or} = M \frac{0.4Gb}{\pi\sqrt{1-v}} \frac{\ln(2\bar{r}/b)}{\lambda_p} \tag{8}$$

where $v = 0.28$ is the Poisson's ratio, $\bar{r} = \sqrt{2/3} \cdot r$ is the mean radius of a circular cross-section in a random plane for spherical precipitates, $r = 0.03$ μm and 0.5 μm are the mean precipitate radii of the 900 °C/1 h and 1100 °C/2 h variants, and λ_p is the inter-precipitates spacing:

$$\lambda_p = 2\bar{r}\left(\sqrt{\frac{\pi}{4f}} - 1\right) \tag{9}$$

where f is the volume fraction of B2 precipitates. The values for f is 0.07 for the 900 °C/1 h variant and 0.19 for the 1100 °C/2 h variant. Using these values as input, the calculated strengthening from the precipitate phase ($\Delta\sigma_P$) are 261 MPa, and 61 MPa for the 900°C/1 h and 1100°C/2 h variants, respectively. All the equations, variables and values adopted for the $Al_{0.6}CoCrFeNi$ HEA in three TMP + HT variants are detailed in Tables 3 and 4.

Table 3. Estimated stress increment of different strengthening mechanisms for CR40, 900 °C/1 h, and 1100 °C/2 h variants.

	σ_0 (MPa)	Solid-Solution Strengthening (MPa)	Dislocation Hardening (MPa)	Grain-Boundary Strengthening (MPa)	Precipitation Hardening (MPa)
Equations	[37]	$M \cdot \frac{G \cdot \varepsilon_s^{3/2} \cdot c^{1/2}}{700}$	$M\alpha Gb\rho^{1/2}$	$k_g \cdot d^{-1/2} + k_t \cdot \lambda^{-1/2}$	$M\frac{0.4Gb}{\pi\sqrt{1-\mu}} \frac{\ln(2\bar{\gamma}/b)}{\lambda_p}$
CR40	162	189	698	159	0
900 °C/1 h	160	133	240	76	261
1100 °C/2 h	158	5	8	85	61

Table 4. Physical meaning and corresponding values for variables used in the strengthening mechanism calculations.

Variables	Meaning	Values	Unit
M	Taylor factor	=3.06 for FCC crystal; =2.75 for BCC crystal	Dimensionless
G	Shear modulus	=67 for FCC phase; =88 for BCC phase	GPa
ε_s	Determined from elastic mismatch and atomic size mismatch	=0.0924 for FCC phase; 5.0599 for BCC phase	Dimensionless
c	Atomic fraction of Al	=12.7, 7.4, and 7.9 for FCC in CR40, 900 °C/1 h, and 1100 °C/2 h; =11.5, 11.9 for BCC in CR40, 900 °C/1 h	Dimensionless
α	Lattice parameter	=0.359 for FCC phase; =0.288 for BCC phase	nm
b	Magnitude of the Burgers vector	=0.254 for FCC phase	nm
ρ	Dislocation density	=10^{12} for FCC phase in CR40; =10^{10} in 900 °C/1 h; =10^8 in 1100 °C/2 h	1/cm^2
k_g	Hall–Petch coefficient	=226 for FCC phase; =617 for BCC phase	MPa $\cdot \sqrt{\mu m}$
k_t	Quasi Hall–Petch coefficient	=226	MPa $\cdot \sqrt{\mu m}$
d	Average grain diameter	=20 for CR40; =14 for 900 °C/1 h; =7 for 1100 °C/2 h	µm
λ	Average twin boundary spacing	=8 for CR40; =3 for 900 °C/1 h; =4 for 1100 °C/2 h	µm
ν	Poison ratio	=0.28	Dimensionless
$\overline{\gamma}$	Mean radius of a circular cross-section in a random plane for spherical particles	=24.495 for 900 °C/1 h; =408.248 for 1100 °C/2 h	nm
λ_p	Inter-precipitates spacing	=115.108 for 900 °C/1 h; =843.559 for 1100 °C/2 h	nm

4.2.6. The Total Nanohardness of Al$_{0.6}$CoCrFeNi in Different States

The rule of mixtures (RoM) is widely used to describe the average property of a composite material:

$$P_{mix} = \sum P_i \cdot V_i \tag{10}$$

where P_{mix} is the total property of the composite material (e.g., hardness, intrinsic yield stresses, etc.), and P_i and V_i are the property and volume fraction of each constituent phase in the material. The overall nanoindentation hardness of both 1 h- and 2 h-annealed HEAs decreased with increased annealing temperature.

4.2.7. Precipitation-Strengthening Calculations Assuming the Shearing Mechanism

For the dislocation-shearing mechanism, three factors should be taken into consideration: The particle-matrix coherency strength ($\Delta\sigma_{cs}$), modulus-mismatch strength ($\Delta\sigma_{ms}$), and atomic-ordering strength ($\Delta\sigma_{os}$) [68].

It is expected that $\Delta\sigma_P = max\{\Delta\sigma_{cs} + \Delta\sigma_{ms}, \Delta\sigma_{os}\}$ [69]. The values of $\Delta\sigma_{cs}$, $\Delta\sigma_{ms}$, and $\Delta\sigma_{os}$ are calculated using Equations (11)–(13):

$$\Delta\sigma_{cs} = M \cdot a_\varepsilon (G \cdot \varepsilon_c)^{3/2} \left(\frac{rf}{0.5Gb}\right)^{3/2} \tag{11}$$

$$\Delta\sigma_{m_S} = M 0.0055 (\Delta G)^{3/2} \left(\frac{2f}{G}\right)^{1/2} \left(\frac{r}{b}\right)^{3m/2-1} \tag{12}$$

$$\Delta\sigma_{os} = M0.81\frac{\gamma_{aqb}}{2b}\left(\frac{3\pi f}{8}\right)^{\frac{1}{2}}\tag{13}$$

where $\alpha_\varepsilon = 2.6$ [70]; $G = 67$ GPa is the shear modulus of the matrix; $\varepsilon_c = 2/3 \cdot \left(\frac{\Delta a}{a}\right) = 0.13$ is the constrained lattice parameter misfit; Δa is the difference of lattice constants between the FCC matrix and particles; a is the lattice constant of FCC phases; $r = 30$ nm is the average radius of precipitates by simplifying as spherical precipitates; f is the volume fraction of the precipitates and determined to be 0.07; ΔG is the modulus mismatch between the matrix and the precipitates and is determined to be $88 - 67 = 21$ GPa; m = 0.85 [22]; $\gamma_{aqb} = 0.12$ J/m^2 is the antiphase boundary free energy of the precipitates referring to the relevant value in Ni-based superalloys [71]. The results of $\Delta\sigma_{cs}$, $\Delta\sigma_{ms}$, and $\Delta\sigma_{os}$ are 103.2 GPa, 0.275 GPa, and 0.168 GPa, respectively, which means that $\Delta\sigma_P$ is 103.4 GPa, and finally determined as 75.5 GPa for the 900 °C/1 h annealed state using RoM. Obviously, this predicted abnormally high stress is not realistic, suggesting that the shearing mechanism is not operative in this alloy at 900 °C/1 h annealed state.

For comparison, the yield stress from predicting theoretical calculations and the experimental results are summarized in Figure 10. As can be seen in Figure 10, the solid-solution strengthening contribution [59–62] is decreasing for variants after annealing, which is attributed to the volume fraction of the FCC phase increasing while the disordered BCC phase is decreasing. As such the change in phase fraction ratio led to the strength loss. The 1100°C/2 h annealed variant thus had the lowest strengthening effect among the three variants. Dislocation strengthening [63] constitutes a major contribution to the yield stress in the CR40 alloy but decreases substantially for the annealed variants due to the dramatic reduction in dislocation densities resulting from annealing heat treatment. Figure 8 also exhibits the calculated results of grain-boundary strengthening [59,63] and secondary-phase hardening [59,68]. Furthermore, for comparing the yield stress predicted from theoretical calculations with the experimental results for Al$_{0.6}$CoCrFeNi HEA in the cold-rolled (CR40) and annealed variants (900 °C/1 h and 1100 °C/2 h). The agreement is acceptable considering the simplicity of those models and the uncertainty associated with determining some of the variables. The agreement can be improved if the parameters or variables can be addressed more precisely in future work.
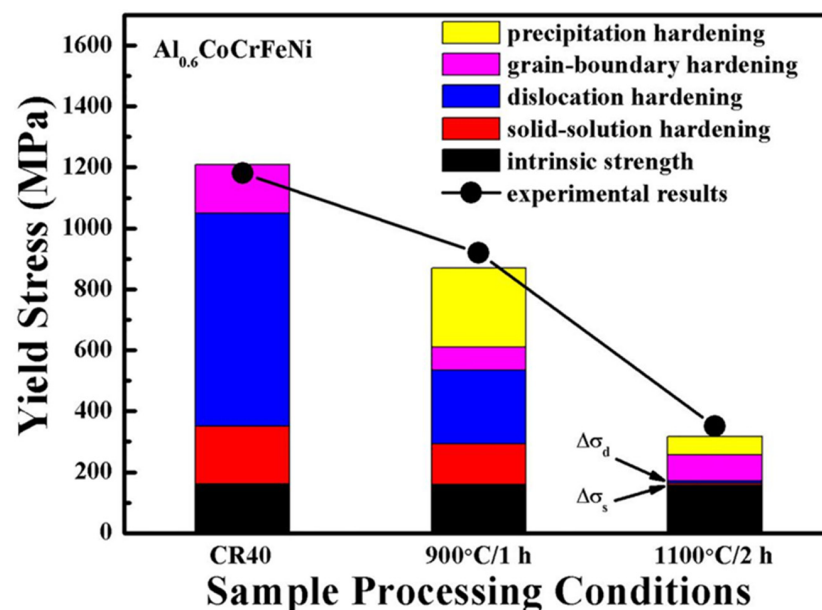

Figure 10. The calculated yield stress agrees well with experimental results for Al$_{0.6}$CoCrFeNi HEA in the CR, 900 °C/1 h, and 1100 °C/2 h variants. The contributions to the yield stress from different strengthening mechanisms are also illustrated.

5. Conclusions

Microstructure evolution, phase stability, and mechanical behavior (i.e., tensile and hardness) of the $Al_{0.6}CoCrFeNi$ HEA subjected to thermo-mechanical treatments were explored in the present work. The following conclusions were drawn:

(1) The as-cast $Al_{0.6}CoCrFeNi$ HEA was composed of FCC matrix, B2, and minor BCC phases. The B2 phase changed its morphology from needle-like to droplet-shaped when annealed at $T \geq 900\ ^\circ C$. The disordered BCC phase disappeared upon annealing. The observed microstructure agrees with the CALPHAD calculation.

(2) The EBSD maps illustrated that cold rolling introduced deformation twins. Recovery and partial recrystallization took place in the $900\ ^\circ C/1\ h$ annealed variant because low-angle grain boundaries remained. The $1100\ ^\circ C/2\ h$ annealed variant was fully recrystallized. This was demonstrated by the predominance of high-angle grain boundaries and the formation of annealing twins.

(3) Nanoindentation hardness tests showed that (1) annealing heat treatments did not affect the nanoindentation hardness of the B2 phase but obviously decreased the hardness of the FCC phase to a more significant extent; and (2) the nanoindentation hardness of BCC/B2 phase is significantly greater than that of the FCC phase.

(4) The yield stress of the cold-rolled $Al_{0.6}CoCrFeNi$ HEA gradually decreased with increased annealing time at a fixed temperature and increased annealing temperature. Annealing at $1000\ ^\circ C$ for $1\ h$ yields an optimal balance of yield stress (886 MPa) and elongation (21%).

(5) Simple models were used to predict the contributions to the yield stress of the FCC and B2/BCC dual-phase $Al_{0.6}CoCrFeNi$ HEA from the solid solution, from dislocation generation and interactions, from grain boundaries and other phase boundaries, and from precipitations and other dispersed phases. A decent agreement was obtained between model prediction and experiment.

References

1. Miracle, D.B.; Senkov, O.N. A critical review of high entropy alloys and related concepts. *Acta Mater.* **2017**, *122*, 448–511. [CrossRef]
2. Micheal, J.-W.Y.; Gao, C.; Liaw, P.K.; Zhang, Y. *High Entropy Alloys Fundamentals and Application*; Springer International Publishing: New York City, NY, USA, 2016.
3. Ye, Y.F.; Wang, Q.; Lu, J.; Liu, C.T.; Yang, Y. High-entropy alloy: Challenges and prospects. *Mater. Today* **2016**, *19*, 349–362. [CrossRef]
4. Zhang, Y.; Zuo, T.T.; Tang, Z.; Gao, M.C.; Dahmen, K.A.; Liaw, P.K.; Lu, Z.P. Microstructures and properties of high-entropy alloys. *Prog. Mater. Sci.* **2014**, *61*, 1–93. [CrossRef]
5. Yeh, J.-W.; Chen, S.K.; Lin, S.-J.; Gan, J.-Y.; Chin, T.-S.; Shun, T.-T.; Tsau, C.-H.; Chang, S.-Y. Nanostructured High-Entropy Alloys with Multiple Principal Elements: Novel Alloy Design Concepts and Outcomes. *Adv. Eng. Mater.* **2004**, *6*, 299–303. [CrossRef]
6. Cantor, B.; Chang, I.T.H.; Knight, P.; Vincent, A.J.B. Microstructural development in equiatomic multicomponent alloys. *Mater. Sci. Eng. A* **2004**, *375–377*, 213–218. [CrossRef]
7. Zhu, C.; Lu, Z.; Nieh, T. Incipient plasticity and dislocation nucleation of FeCoCrNiMn high-entropy alloy. *Acta Mater.* **2013**, *61*, 2993–3001. [CrossRef]
8. Ma, Y.; Wang, Q.; Jiang, B.; Li, C.; Hao, J.; Li, X.; Dong, C.; Nieh, T. Controlled formation of coherent cuboidal nanoprecipitates in body-centered cubic high-entropy alloys based on $Al_2(Ni,Co,Fe,Cr)_{14}$ compositions. *Acta Mater.* **2018**, *147*, 213–225. [CrossRef]
9. Zhao, Y.; Qiao, J.; Ma, S.; Gao, M.; Yang, H.; Chen, M.; Zhang, A. A hexagonal close-packed high-entropy alloy: The effect of entropy. *Mater. Des.* **2016**, *96*, 10–15. [CrossRef]
10. Gludovatz, B.; Hohenwarter, A.; Catoor, D.; Chang, E.H.; George, E.P.; Ritchie, R.O. A fracture-resistant high-entropy alloy for cryogenic applications. *Science* **2014**, *345*, 1153–1158. [CrossRef] [PubMed]
11. Shi, Y.; Yang, B.; Xie, X.; Brechtl, J.; Dahmen, K.A.; Liaw, P.K. Corrosion of $Al_xCoCrFeNi$ high-entropy alloys: Al-content and potential scan-rate dependent pitting behavior. *Corros. Sci.* **2017**, *119*, 33–45. [CrossRef]
12. Senkov, O.N.; Wilks, G.B.; Miracle, D.B.; Chuang, C.P.; Liaw, P.K. Refractory high-entropy alloys. *Intermetallics* **2010**, *18*, 1758–1765. [CrossRef]
13. Chuang, M.-H.; Tsai, M.-H.; Wang, W.-R.; Lin, S.-J.; Yeh, J.-W. Microstructure and wear behavior of $Al_xCo_{1.5}CrFeNi_{1.5}Tiy$ high-entropy alloys. *Acta Mater.* **2011**, *59*, 6308–6317. [CrossRef]
14. Hemphill, M.; Yuan, T.; Wang, G.; Yeh, J.; Tsai, C.; Chuang, A.; Liaw, P. Fatigue behavior of $Al_{0.5}CoCrCuFeNi$ high entropy alloys. *Acta Mater.* **2012**, *60*, 5723–5734. [CrossRef]
15. von Rohr, F.; Winiarski, M.; Tao, J.; Klimczuk, T.; Cava, R.J. Effect of electron count and chemical complexity in the Ta-Nb-Hf-Zr-Ti high-entropy alloy superconductor. *Proc. Natl. Acad. Sci. USA* **2016**, *113*, E7144–E7150. [CrossRef]
16. Gao, M.C.; Zhang, C.; Gao, P.; Zhang, F.; Ouyang, L.Z.; Widom, M.; Hawk, J.A. Thermodynamics of concentrated solid solution alloys. *Curr. Opin. Solid State Mater. Sci.* **2017**, *21*, 238–251. [CrossRef]
17. Yang, X.; Zhang, Y. Prediction of high-entropy stabilized solid-solution in multi-component alloys. *Mater. Chem. Phys.* **2012**, *132*, 233–238. [CrossRef]
18. Zhang, Y.; Zhou, Y.J.; Lin, J.P.; Chen, G.L.; Liaw, P.K. Solid-Solution Phase Formation Rules for Multi-component Alloys. *Adv. Eng. Mater.* **2008**, *10*, 534–538. [CrossRef]
19. Ma, L.; Wang, L.; Nie, Z.; Wang, F.; Xue, Y.; Zhou, J.; Cao, T.; Wang, Y.; Ren, Y. Reversible deformation-induced martensitic transformation in $Al_{0.6}CoCrFeNi$ high-entropy alloy investigated by in situ synchrotron-based high-energy X-ray diffraction. *Acta Mater.* **2017**, *128*, 12–21. [CrossRef]
20. Lim, K.R.; Lee, K.S.; Lee, J.S.; Kim, J.Y.; Chang, H.J.; Na, Y.S. Dual-phase high-entropy alloys for high-temperature structural applications. *J. Alloys Compd.* **2017**, *728*, 1235–1238. [CrossRef]
21. Otto, F.; Dlouhý, A.; Somsen, C.; Bei, H.; Eggeler, G.; George, E.P. The influences of temperature and microstructure on the tensile properties of a CoCrFeMnNi high-entropy alloy. *Acta Mater.* **2013**, *61*, 5743–5755. [CrossRef]
22. He, J.Y.; Wang, H.; Huang, H.L.; Xu, X.D.; Chen, M.W.; Wu, Y.; Liu, X.J.; Nieh, T.G.; An, K.; Lu, Z.P. A precipitation-hardened high-entropy alloy with outstanding tensile properties. *Acta Mater.* **2016**, *102*, 187–196. [CrossRef]
23. Yasuda, H.Y.; Miyamoto, H.; Cho, K.; Nagase, T. Formation of ultrafine-grained microstructure in $Al_{0.3}CoCrFeNi$ high entropy alloys with grain boundary precipitates. *Mater. Lett.* **2017**, *199*, 120–123. [CrossRef]
24. Klimova, M.; Stepanov, N.; Shaysultanov, D.; Chernichenko, R.; Yurchenko, N.; Sanin, V.; Zherebtsov, S. Microstructure and Mechanical Properties Evolution of the Al, C-Containing CoCrFeNiMn-Type High-Entropy Alloy during Cold Rolling. *Materials* **2018**, *11*, 53. [CrossRef]
25. Li, D.; Li, C.; Feng, T.; Zhang, Y.; Sha, G.; Lewandowski, J.; Liaw, P.K. High-entropy $Al_{0.3}CoCrFeNi$ alloy fibers with high tensile strength and ductility at ambient and cryogenic temperatures. *Acta Mater.* **2017**, *123*, 285–294. [CrossRef]
26. Joseph, J.; Stanford, N.; Hodgson, P.; Fabijanic, D. Tension/compression asymmetry in additive manufactured face centered cubic high entropy alloy. *Scr. Mater.* **2017**, *129*, 30–34. [CrossRef]
27. Joseph, J.; Stanford, N.; Hodgson, P.; Fabijanic, D.M. Understanding the mechanical behaviour and the large strength/ductility differences between FCC and BCC $Al_xCoCrFeNi$ high entropy alloys. *J. Alloys Compd.* **2017**, *726*, 885–895. [CrossRef]
28. Kumar, N.; Ying, Q.; Nie, X.; Mishra, R.; Tang, Z.; Liaw, P.; Brennan, R.; Doherty, K.; Cho, K. High strain-rate compressive deformation behavior of the $Al_{0.1}CrFeCoNi$ high entropy alloy. *Mater. Des.* **2015**, *86*, 598–602. [CrossRef]

29. Kao, Y.-F.; Chen, T.-J.; Chen, S.-K.; Yeh, J.-W. Microstructure and mechanical property of as-cast, -homogenized, and -deformed AlxCoCrFeNi ($0 \leq x \leq 2$) high-entropy alloys. *J. Alloys Compd.* **2009**, *488*, 57–64. [CrossRef]

30. CompuTherm. 2018. Available online: http://www.computherm.com/ (accessed on 20 September 2021).

31. Scheil, E. Commments on the layer crystal formation. *Z. Für Met.* **1942**, *34*, 70–72.

32. Wang, W.-R.; Wang, W.-L.; Wang, S.-C.; Tsai, Y.-C.; Lai, C.-H.; Yeh, J.-W. Effects of Al addition on the microstructure and mechanical property of Al$_x$CoCrFeNi high-entropy alloys. *Intermetallics* **2012**, *26*, 44–51. [CrossRef]

33. Wang, W.-R.; Wang, W.-L.; Yeh, J.-W. Phases, microstructure and mechanical properties of Al$_x$CoCrFeNi high-entropy alloys at elevated temperatures. *J. Alloys Compd.* **2014**, *589*, 143–152. [CrossRef]

34. Li, Z.; Tasan, C.C.; Pradeep, K.G.; Raabe, D. A TRIP-assisted dual-phase high-entropy alloy: Grain size and phase fraction effects on deformation behavior. *Acta Mater.* **2017**, *131*, 323–335. [CrossRef]

35. Askeland, D.R. *The Science and Engineering of Materials*; Springer International Publishing: New York City, NY, USA, 2003.

36. Wu, Y.; Cai, Y.; Wang, T.; Si, J.; Zhu, J.; Wang, Y.; Hui, X. A refractory Hf$_{25}$Nb$_{25}$Ti$_{25}$Zr$_{25}$ high-entropy alloy with excellent structural stability and tensile properties. *Mater. Lett.* **2014**, *130*, 277–280. [CrossRef]

37. Juan, C.-C.; Tsai, M.-H.; Tsai, C.-W.; Hsu, W.-L.; Lin, C.-M.; Chen, S.-K.; Lin, S.-J.; Yeh, J.-W. Simultaneously increasing the strength and ductility of a refractory high-entropy alloy via grain refining. *Mater. Lett.* **2016**, *184*, 200–203. [CrossRef]

38. Tang, Z.; Senkov, O.N.; Parish, C.; Zhang, C.; Zhang, F.; Santodonato, L.; Wang, G.; Zhao, G.; Yang, F.; Liaw, P.K. Tensile ductility of an AlCoCrFeNi multi-phase high-entropy alloy through hot isostatic pressing (HIP) and homogenization. *Mater. Sci. Eng. A* **2015**, *647*, 229–240. [CrossRef]

39. Lilensten, L.; Couzinié, J.-P.; Bourgon, J.; Perrière, L.; Dirras, G.; Prima, F.; Guillot, I. Design and tensile properties of a bcc Ti-rich high-entropy alloy with transformation-induced plasticity. *Mater. Res. Lett.* **2016**, *5*, 110–116. [CrossRef]

40. Liu, W.; He, J.; Huang, H.; Wang, H.; Lu, Z.; Liu, C.T. Effects of Nb additions on the microstructure and mechanical property of CoCrFeNi high-entropy alloys. *Intermetallics* **2015**, *60*, 1–8. [CrossRef]

41. Chen, J.; Yao, Z.; Wang, X.; Lu, Y.; Wang, X.; Liu, Y.; Fan, X. Effect of C content on microstructure and tensile properties of as-cast CoCrFeMnNi high entropy alloy. *Mater. Chem. Phys.* **2018**, *210*, 136–145. [CrossRef]

42. Shun, T.-T.; Du, Y.-C. Microstructure and tensile behaviors of FCC Al$_{0.3}$CoCrFeNi high entropy alloy. *J. Alloys Compd.* **2009**, *479*, 157–160. [CrossRef]

43. Ma, S.; Qiao, J.; Wang, Z.; Yang, H.; Zhang, Y. Microstructural features and tensile behaviors of the Al$_{0.5}$CrCuFeNi$_2$ high-entropy alloys by cold rolling and subsequent annealing. *Mater. Des.* **2015**, *88*, 1057–1062. [CrossRef]

44. Chen, L.; Wei, R.; Tang, K.; Zhang, J.; Jiang, F.; Sun, J. Ductile-brittle transition of carbon alloyed Fe$_{40}$Mn$_{40}$Co$_{10}$Cr$_{10}$ high entropy alloys. *Mater. Lett.* **2019**, *236*, 416–419. [CrossRef]

45. Wang, Z.; Gao, M.C.; Ma, S.G.; Yang, H.J.; Wang, Z.H.; Ziomek-Moroz, M.; Qiao, J.W. Effect of cold rolling on the microstructure and mechanical properties of Al$_{0.25}$CoCrFe$_{1.25}$Ni$_{1.25}$ high-entropy alloy. *Mater. Sci. Eng. A* **2015**, *645*, 163–169. [CrossRef]

46. Wani, I.S.; Bhattacharjee, T.; Sheikh, S.; Lu, Y.P.; Chatterjee, S.; Bhattacharjee, P.P.; Guo, S.; Tsuji, N. Ultrafine-Grained AlCoCrFeNi$_{2.1}$ Eutectic High-Entropy Alloy. *Mater. Res. Lett.* **2016**, *4*, 174–179. [CrossRef]

47. Jin, X.; Zhou, Y.; Zhang, L.; Du, X.; Li, B. A novel Fe$_{20}$Co$_{20}$Ni$_{41}$Al$_{19}$ eutectic high entropy alloy with excellent tensile properties. *Mater. Lett.* **2018**, *216*, 144–146. [CrossRef]

48. He, J.; Liu, W.; Wang, H.; Wu, Y.; Liu, X.; Nieh, T.; Lu, Z. Effects of Al addition on structural evolution and tensile properties of the FeCoNiCrMn high-entropy alloy system. *Acta Mater.* **2014**, *62*, 105–113. [CrossRef]

49. Gutierrez-Urrutia, I.; Zaefferer, S.; Raabe, D. The effect of grain size and grain orientation on deformation twinning in a Fe–22wt.% Mn–0.6wt.% C TWIP steel. *Mater. Sci. Eng. A* **2010**, *527*, 3552–3560. [CrossRef]

50. Yang, H.K.; Zhang, Z.J.; Tian, Y.Z.; Zhang, Z.F. Negative to positive transition of strain rate sensitivity in Fe-22Mn-0.6C-x(Al) twinning-induced plasticity steels. *Mater. Sci. Eng. A* **2017**, *690*, 146–157. [CrossRef]

51. Grässel, L.K.O.; Frommeyer, G.; Meyer, L.W. High strength Fe-Mn-(Al, Si) TRIP TWIP steels development, properties, application. *Int. J. Plast.* **2000**, *16*, 1391–1409. [CrossRef]

52. Wu, Z.; Parish, C.; Bei, H. Nano-twin mediated plasticity in carbon-containing FeNiCoCrMn high entropy alloys. *J. Alloys Compd.* **2015**, *647*, 815–822. [CrossRef]

53. Chen, X.-M.; Lin, Y.; Wu, F. EBSD study of grain growth behavior and annealing twin evolution after full recrystallization in a nickel-based superalloy. *J. Alloys Compd.* **2017**, *724*, 198–207. [CrossRef]

54. Christian, J.W.; Mahajan, S. Deformation Twinning. *Prog. Mater. Sci.* **1995**, *39*, 1–157. [CrossRef]

55. Mahajan, S.; Pande, C.S.; Imam, M.A.; Rath, B.B. Formation of annealing twins in f.c.c. crystals. *Acta Mater.* **1997**, *45*, 2633–2638. [CrossRef]

56. Rao, J.C.; Diao, H.Y.; Ocelík, V.; Vainchtein, D.; Zhang, C.; Kuo, C.; Tang, Z.; Guo, W.; Poplawsky, J.D.; Zhou, Y.; et al. Secondary phases in Al x CoCrFeNi high-entropy alloys: An in-situ TEM heating study and thermodynamic appraisal. *Acta Mater.* **2017**, *131*, 206–220. [CrossRef]

57. Bönisch, M.; Wu, Y.; Sehitoglu, H. Twinning-induced strain hardening in dual-phase FeCoCrNiAl$_{0.5}$ at room and cryogenic temperature. *Sci. Rep.* **2018**, *8*, 10663. [CrossRef]

58. Ma, K.; Wen, H.; Hu, T.; Topping, T.D.; Isheim, D.; Seidman, D.N.; Lavernia, E.J.; Schoenung, J.M. Mechanical behavior and strengthening mechanisms in ultrafine grain precipitation-strengthened aluminum alloy. *Acta Mater.* **2014**, *62*, 141–155. [CrossRef]

59. Wen, H.; Topping, T.D.; Isheim, D.; Seidman, D.N.; Lavernia, E.J. Strengthening mechanisms in a high-strength bulk nanostructured Cu–Zn–Al alloy processed via cryomilling and spark plasma sintering. *Acta Mater.* **2013**, *61*, 2769–2782. [CrossRef]

60. Schuh, C.; Nieh, T.; Iwasaki, H. The effect of solid solution W additions on the mechanical properties of nanocrystalline Ni. *Acta Mater.* **2003**, *51*, 431–443. [CrossRef]

61. Toda-Caraballo, I. A general formulation for solid solution hardening effect in multicomponent alloys. *Scr. Mater.* **2017**, *127*, 113–117. [CrossRef]

62. Toda-Caraballo, I.; Rivera-Díaz-Del-Castillo, P.E. Modelling solid solution hardening in high entropy alloys. *Acta Mater.* **2015**, *85*, 14–23. [CrossRef]

63. Courtney, T.H. Mechanical Behavior of Materials. *Mater. Today* **2009**, *12*, 44.

64. Meyers, M.A.; Chawla, K.K. *Mechanical Behavior of Materials*; Cambridge University Press: Cambridge, UK, 2008.

65. Lu, Y.; Gao, X.; Jiang, L.; Chen, Z.; Wang, T.; Jie, J.; Kang, H.; Zhang, Y.; Guo, S.; Ruan, H.; et al. Directly cast bulk eutectic and near-eutectic high entropy alloys with balanced strength and ductility in a wide temperature range. *Acta Mater.* **2017**, *124*, 143–150. [CrossRef]

66. Liu, W.; Wu, Y.; He, J.; Nieh, T.; Lu, Z. Grain growth and the Hall–Petch relationship in a high-entropy FeCrNiCoMn alloy. *Scr. Mater.* **2013**, *68*, 526–529. [CrossRef]

67. Heo, N.H.; Heo, Y.-U.; Kwon, S.K.; Kim, N.J.; Kim, S.-J.; Lee, H.-C. Extended Hall–Petch Relationships for Yield, Cleavage and Intergranular Fracture Strengths of bcc Steel and Its Deformation and Fracture Behaviors. *Met. Mater. Int.* **2018**, *24*, 265–281. [CrossRef]

68. Seidman, D.N.; Marquis, E.A.; Dunand, D.C. Precipitation strengthening at ambient and elevated temperatures of heat-treatable Al(Sc) alloys. *Acta Mater.* **2002**, *50*, 4021–4035. [CrossRef]

69. Booth-Morrison, C.; Dunand, D.C.; Seidman, D.N. Coarsening resistance at 400 °C of precipitation-strengthened Al–Zr–Sc–Er alloys. *Acta Mater.* **2011**, *59*, 7029–7042. [CrossRef]

70. Ardell, A.J. Precipitation hardening. *Metall. Trans. A* **1985**, *10*, 151–391. [CrossRef]

71. Pollock, A.A.T. Creep resistance of CMSX-3 nickel base superalloy single crystals. *Acta Metall. Mater.* **1992**, *40*, 1–30. [CrossRef]